



**HAL**  
open science

## **bacto\_tracker: a method for single-cell tracking of *M. xanthus* in dense and multispecies colonies**

Sara Rombouts, Jean-Bernard Fiche, Tam Mignot, Marcelo Nollmann

### ► To cite this version:

Sara Rombouts, Jean-Bernard Fiche, Tam Mignot, Marcelo Nollmann. bacto\_tracker: a method for single-cell tracking of *M. xanthus* in dense and multispecies colonies. Open Research Europe, 2022, 2, pp.136. 10.12688/openreseurope.15255.1 . hal-04216509

**HAL Id: hal-04216509**

**<https://hal.umontpellier.fr/hal-04216509>**

Submitted on 25 Sep 2023


**HAL** is a multi-disciplinary open access archive for the deposit and dissemination of scientific research documents, whether they are published or not. The documents may come from teaching and research institutions in France or abroad, or from public or private research centers.

L'archive ouverte pluridisciplinaire **HAL**, est destinée au dépôt et à la diffusion de documents scientifiques de niveau recherche, publiés ou non, émanant des établissements d'enseignement et de recherche français ou étrangers, des laboratoires publics ou privés.



METHOD ARTICLE

# bacto\_tracker: a method for single-cell tracking of *M. xanthus* in dense and multispecies colonies [version 1; peer review: awaiting peer review]

Sara Rombouts<sup>1</sup>, Jean-Bernard Fiche<sup>1</sup>, Tam Mignot<sup>2</sup>, Marcelo Nollmann <sup>1</sup><sup>1</sup>Centre de Biologie Structurale, Univ Montpellier, CNRS UMR5048, INSERM U1054, Montpellier, 34090, France<sup>2</sup>Laboratoire de Chimie Bactérienne, Centre National de la Recherche Scientifique, Marseille, France

**V1** First published: 09 Dec 2022, 2:136  
<https://doi.org/10.12688/openreseurope.15255.1>

Latest published: 09 Dec 2022, 2:136  
<https://doi.org/10.12688/openreseurope.15255.1>

## Open Peer Review

**Approval Status** AWAITING PEER REVIEW

Any reports and responses or comments on the article can be found at the end of the article.

## Abstract

Cell motility and predation are important for the dynamics of many multi-cellular ecosystems, such as the gut or the soil. Approaches to image cell dynamics in such complex systems are scant, and high-throughput analysis methods to segment and track single-cell behaviors are currently lacking. Here, we addressed these limitations by implementing a fast fluorescence microscopy technique enabling the high-resolution acquisition of cell movement over large areas and long time periods. Next, we applied deep learning to semantically segment two different bacteria species within complex micro-environments. We implemented a method to build single cell traces by combining the cell masks from different time points to follow the dynamics of single cells with high spatial and temporal resolutions and over long periods of time. We applied and validated these methods by characterizing the dynamics of *Escherichia coli* predation by *Myxococcus xanthus*.

## Keywords

time-lapse imaging, biofilm, deep-learning



This article is included in the [Cell, Molecular and Structural Biology](#) gateway.



This article is included in the [European Research Council \(ERC\)](#) gateway.



This article is included in the [Microbiology gateway](#).



This article is included in the [Marie-Sklodowska-Curie Actions \(MSCA\) gateway](#).



This article is included in the [Bacterial Pathogenesis collection](#).

**Corresponding author:** Marcelo Nollmann ([marcnol@gmail.com](mailto:marcnol@gmail.com))

**Author roles:** **Rombouts S:** Conceptualization, Data Curation, Formal Analysis, Methodology, Resources, Software, Validation, Visualization, Writing – Original Draft Preparation, Writing – Review & Editing; **Fiche JB:** Conceptualization, Data Curation, Formal Analysis, Methodology, Resources, Software, Supervision, Validation, Visualization, Writing – Review & Editing; **Mignot T:** Conceptualization, Resources, Writing – Review & Editing; **Nollmann M:** Conceptualization, Funding Acquisition, Supervision, Writing – Original Draft Preparation, Writing – Review & Editing

**Competing interests:** No competing interests were disclosed.

**Grant information:** This research was financially supported by the European Research Council (ERC) under the European Union's Horizon 2020 Research and Innovation Programme (grant agreement Nos 724429 and 885145); the European Union's Horizon 2020 Research and Innovation Program no 885145 (A Multiscale Analysis of Bacterial Predation [JAWS]); the Marie Skłodowska-Curie Grant Agreement No 721874 (Scanning probe microscopies for nanoscale fast, tomographic and composition imaging [SPM2.0]); and the Bettencourt-Schueller Foundation for their prize 'Coup d'élan pour la recherche Française', and the France-BioImaging infrastructure supported by the French National Research Agency (grant ID ANR-10-INBS-04, "Investments for the Future").

*The funders had no role in study design, data collection and analysis, decision to publish, or preparation of the manuscript.*

**Copyright:** © 2022 Rombouts S *et al.* This is an open access article distributed under the terms of the [Creative Commons Attribution License](#), which permits unrestricted use, distribution, and reproduction in any medium, provided the original work is properly cited.

**How to cite this article:** Rombouts S, Fiche JB, Mignot T and Nollmann M. **bacto\_tracker: a method for single-cell tracking of *M. xanthus* in dense and multispecies colonies [version 1; peer review: awaiting peer review]** Open Research Europe 2022, 2:136 <https://doi.org/10.12688/openreseurope.15255.1>

**First published:** 09 Dec 2022, 2:136 <https://doi.org/10.12688/openreseurope.15255.1>

## Plain language summary

The function of cells in many contexts require that they move and explore their surroundings. An excellent example is the movement of bacterial cells in their natural habitats, such as the forest floor or the gut. *Myxococcus xanthus* is a bacterial species that moves as large cell groups in search of food. In this process, they can kill and prey on other bacterial species. The study of how single cells move and prey on other bacteria has been prevented by the lack of acquisition and analysis tools able to follow the fast dynamics and to detect single bacterial cells in crowded environments. We have addressed this limitation by developing a microscopy method that enables the fast acquisition of different bacterial species over large areas. We combined this detection with an analysis method relying on artificial intelligence that is able to segment single predator and prey cells in their natural ecosystems. We implemented a technique that joins these single cells together to build a trajectory that allows researchers to characterize the collective and single cell movement of cells during bacterial predation. Finally, we have demonstrated the use of these technologies during the predation of *Escherichia coli* predation by *Myxococcus xanthus*.

## Introduction

Cell motility is essential for many biological processes, such as tissue remodeling, development, or the immune response to pathogens. Cell motility in complex multi-cellular environments is controlled by external signals at the level of the organism (Devi *et al.*, 2021; Jacobson *et al.*, 2021), or locally by cell-cell interactions. These interactions are particularly important during predation, where cell movement needs to be halted to deploy killing strategies (Nauseef & Borregaard, 2014). A fascinating example of this coupling between motility and predation was recently reported for the process of bacterial predation by *Myxococcus xanthus* (*M. xanthus*) (Seef *et al.*, 2021).

*M. xanthus* is a gram-negative bacterium that lives in the soil. To survive in this complex ecosystem, it has developed a social lifestyle based on its capacity to move over a surface in a collective and coordinated manner (Dworkin, 1963; Zhang *et al.*, 2012). This motility allows *M. xanthus* to create hunting packs able to seek prey on centimeter-scale distances, or to induce collective motion towards aggregation centers to form spore-filled fruiting bodies (Muñoz-Dorado *et al.*, 2016). Both phenomena, predation and fruiting body formation, exceed the length scales of the single cell and arise from the strong coordinated dynamics of individual cells (Zhang *et al.*, 2012). The process of *M. xanthus* predation occurs in several phases: i) exploration of the environment in search for nutrients, ii) encountering of prey, iii) progression of dense swarms to regions where prey is found, iv) killing of prey, and v) take-up of nutrients (Keane & Berleman, 2016). The occurrence of these cellular behaviors suggest that they all contribute to successful and efficient predation. However, it remains unclear how and to what extent intra- and inter-cellular behaviors affect this complex process.

Due to experimental and technical constraints, it has been challenging to study single cell behavior within the macroscopic context of bacterial predation. First, bacterial predation between *M. xanthus* and *Escherichia coli* (*E. coli*) is a colony-phenomenon (>1mm) that exceeds the length scales accessible with high-resolution microscopy imaging (<1µm). Therefore, it is challenging to capture an area that is large enough to provide colony-wide context while being able to resolve single bacterial cells. Second, even if a large area could be microscopically captured, *M. xanthus* cells aggregate into densely packed swarms during colony expansion, and *E. coli* cells are tightly-packed at the colony periphery or at micro-colonies or 'islands' (in our conditions these have a typical size of 30µm). To automatically segment cells in such dense conditions is challenging with classical methods, particularly when working with low-phototoxicity imaging conditions such as brightfield or low-intensity fluorescence. Several software packages for cell segmentation have recently become available, such as SuperSegger (Stylianidou *et al.*, 2016), Oufiti (Paintdakhi *et al.*, 2016) and MicrobeJ (Ducret *et al.*, 2016). However, these methods are ill suited for simultaneous segmentation of multiple bacterial species, dense bio-films and low-contrast imaging modalities (e.g., brightfield). Recently, artificial-intelligence (AI) based solutions for semantic cell segmentation of complex microbial communities were proposed that can efficiently segment and identify multiple species in millimeter-sized static images (Panigrahi *et al.*, 2021). These methods permit the semantic segmentation of cells from static images, but do not enable the dynamic tracking of different bacterial species or collective groups with single-cell resolution.

Cells within microbial communities are constantly in motion, thus understanding the mechanisms involved in biofilm development, resource consumption, or predation requires tools able to track the movement of cells within different cell groups in space and time. For instance, *M. xanthus* predation of *E. coli* is an inherently dynamic process whereby *M. xanthus* cells glide towards and within *E. coli* colonies that disappear over time as a result of their lysis. Semantic single-cell tracking within complex microbial communities requires a method with the ability to follow cells from different species, over relevant periods of time (typically several hours), at relevant spatial scales (~ 0.1–1mm<sup>2</sup>), and with enough time resolution to identify single cell trajectories in crowded environments (typically tens of seconds). This study is based on the PhD thesis of the first named author available here (Rombouts, 2021).

Here, we present a method that addresses these challenges. First, we developed a hardware-accelerated, automated microscope to robustly image large areas of the sample (~0.4mm<sup>2</sup>), over long periods of time (>6h), and with high temporal resolution (~30s/image). Second, we applied a deep-learning approach to semantically segment single cells within densely-packed cell groups. Third, we designed a cell tracking algorithm to track single motile cells. Finally, we extracted



dynamic track parameters from thousands of single-cell tracks with spatial resolution.

## Methods

### Bacterial cultures

The bacterial strains used in this work can be found in Underlying Table 1 (Nollmann, 2022a). *E. coli* cells used in predation assays were grown overnight in 10 ml Luria-Bertani (LB) medium at 32°C under agitation (200 rpm). To ensure that *E. coli* cells were in exponential phase after overnight growth, a 1:10 dilution of the starter culture was made in fresh LB medium and incubated for approximately four hours. *M. xanthus* cells were grown overnight in 10 ml Casitone Yeast Extract (CYE) rich medium as was described before (Bustamante *et al.*, 2004) at 32°C under agitation (200 rpm), supplemented with antibiotics (Ampicillin 1 µg/ml) when necessary. Cells were harvested when the OD<sub>600</sub> reached 0.1–0.5.

### Predation assays

Bacterial predation was established in laboratory conditions by setting up a predation assay. In short, *E. coli* and *M. xanthus* cells were harvested from the LB and CYE media, respectively. Cells were concentrated by centrifugation on a tabletop centrifuge at 2100 g for 5 min at room temperature and resuspended in CF medium (10 mM MOPS (pH 7.6), 1 mM KH<sub>2</sub>PO<sub>4</sub>, 8 mM MgSO<sub>4</sub>, 0.02% (NH<sub>4</sub>)<sub>2</sub>SO<sub>4</sub>, 0.2% sodium citrate, 0.015% bacto casitone peptone). *M. xanthus* cells were concentrated to an OD<sub>600</sub> of 5, *E. coli* cells were concentrated to an OD<sub>600</sub> of 0.005. Cell suspensions of 1 µl were spotted at close distance of approximately 1 mm on CF 1.5% agar pads supported on a coverslip.

The agar pads used for time lapse imaging were made with ultrapure agar (UltraPure Agarose 1000, Invitrogen) to limit autofluorescence by impurities in the agar solutions. To limit any background signal during high resolution fluorescence imaging, the agar pad was made as thin as possible. In short, pads were made by pipetting 550 µl of melted agar onto a 25mm coverslip and by placing a second coverslip on the drop of agar, allowing the latter to solidify between two flat surfaces. Once the agar pad was made, the top coverslip was removed and the agar was cut to a diameter of 20 mm.

The prepared predation assays were then placed onto a layer of CF 1.5% agar in a petri dish and the petri dish was closed with parafilm to avoid agar pad evaporation and drying. Samples were incubated 24h to 48h at 32°C to allow *M. xanthus* cells to invade the *E. coli* colony.

### Microscopy

Time lapse imaging was performed on a homemade fully-automated hardware-accelerated wide-field epifluorescence microscope built on a rapid automated modular microscope (RAMM) system (Applied Scientific Instrumentation). Samples were imaged using a 60x Plan-Achromat water-immersion objective (NA = 1.2, Nikon, Japan). The objective lens was mounted on a closed-loop piezoelectric stage (Nano-F100,

Mad City Labs Inc. - USA). Illumination was provided by a brightfield illumination source and 2 lasers (OBIS-488 nm and Sapphire-LP-561 nm, Coherent – USA). Images were acquired using a sCMOS camera (ORCA Flash 4.0V3, Hamamatsu – Japan), with a final pixel size calibrated to 106 nm. A custom-built autofocus system was used to correct for axial drift in real-time and maintain the sample in focus. Software-controlled microscope components, including camera, stages, brightfield illumination and lasers were run using a custom-made software package developed in LabView 2015 (National Instrument).

### Fast time lapse imaging

For imaging of the predation assay, the sample was covered with an imaging coverslip. The imaging coverslip was washed consecutively with acetone, Milli-Q water, 70% ethanol (v/v), and Milli-Q water, and flamed to remove any fluorescence impurities and residues. The coverslip was cooled down to room temperature and placed hermetically on the sample while avoiding bubbles between the sample and the coverslip. The sample was mounted in an open attofluor and onto the microscope for imaging. A region of interest spanning an area of approximately 0.36 mm<sup>2</sup> was selected. This large area was imaged by acquiring a mosaic patchwork of 3 by 3 fields of view (FOVs) of 2048x2048 pixels each. An overlap of 160 pixels between consecutive tiles was allowed for image registration. An imaging cycle, in which the 3-by-3 mosaic was imaged by sample displacement following a serpentine pattern, was thus made up of 9 consecutive acquisitions. For each FOV, a 3D-stack was acquired to account for sample tilt in brightfield and in the fluorescence channel of 561 nm for *E. coli* carrying a HU-mCherry fusion. An additional fluorescent channel was added for *M. xanthus* when the used strain was carrying a fluorescent protein as well. A 3D-stack was generally made up of 7–12 planes interspaced with 250–500 nm. Exposure time was set at 50 ms. The laser powers used were kept at low intensity to limit phototoxic effects on the live cells during time lapse acquisition. Imaging cycles were generally completed in 30–40 seconds and were repeated 700 times to construct an hours-long time lapse series of the mosaic area.

### Treatment of fast time lapse data

The full pipeline of analysis, including script names, as well as inputs and outputs are included in underlying Table 2 (Nollmann, 2022a). To increase imaging speed, all images from one imaging cycle were pooled into one DCIMG file. First, the DCIMG files were converted to tiff files with software from Hamamatsu and sorted for each FOV, channel and time point. Tiff images of the fluorescent channel of *E. coli* were deconvolved with Huygens Professional version 20.04 (Scientific Volume Imaging, the Netherlands, <https://svi.nl/>). Deconvolved *E. coli* stacks were z-projected by calculating the standard deviation. 3D brightfield stacks were converted to 2D images by dividing each stack in 16 ROIs of 512x512 pixels, selecting automatically or manually the in-focus plane for each ROI and restitching the 16 ROIs. The code for

calculating the in-focus brightfield image was implemented in *bacto\_tracker/im\_straighter.m* and *bacto\_tracker/im\_straighter\_manual.m*. 2D brightfield and *E. coli* fluorescence images were used as input for a custom MATLAB script using a convolutional neural network with U-Net architecture for semantic segmentation (Ronneberger *et al.*, 2015; Van Valen *et al.*, 2016). Semantic segmentation was performed with five independently trained networks to converge towards a high confidence result, outputting an image with pixel values representing the pixel assignment confidence to a given class. The code for semantic segmentation was implemented in *bacto\_tracker/segment.m*. The final database was used to independently train five networks. The trained networks can be found in *bacto\_tracker/Trained\_networks*.

Segmented images were then used to reconstruct the mosaic image by tiling the 9 images. Exact image overlap for tiling was calculated by image-based pixel-resolution cross correlation. Drift in time was corrected by aligning the mosaic images based on cross correlation calculated from segmented images of stationary *E. coli* microcolonies. *M. xanthus* segments from mosaic images were post-processed to reduce segmentation artifacts. In short, binary masks were generated from the masks by exploiting the assignment of confidence values, masks were filtered for size and finally, tortuous masks and fused masks were rejected. *E. coli* masks were post-processed to avoid overlap between *E. coli* and *M. xanthus* masks and filtered for size to reject isolated pixels. Drift correction cross-correlation was implemented in *bacto\_tracker/mosaic\_drift\_correction.py*, tile calculation in *tile\_calculation.py*, and mosaic assembly for bright field and fluorescence images in *bacto\_tracker/builds\_mosaic.m*.

### Training data set

A large, diverse and representative training data set was constructed consisting of three sets of images: i) brightfield images, ii) their respective *E. coli* fluorescence images, and iii) their respective manually annotated ground truth images. The ground truth consisted of 5 classes: i) background, ii) *E. coli* cell body, iii) *E. coli* contour, iv) *M. xanthus* cell body, and v) *M. xanthus* contour.

### Single cell tracking

Single cell trajectories were reconstructed with an in-house developed MATLAB pipeline. For each timepoint in the time lapse image series, pairwise tracks were constructed between cells in frame *k* and cells in frame *k+1*. Briefly, the enlarged bounding box of the cell mask in frame *k* was utilized to select a number of possible candidates in frame *k+1*. Ultimately, the optimal candidate was found by ranking the candidates with Analytical Hierarchy Processing (AHP) (Saaty, 1986) based on several parameters of the masks including cell area, cell length, and mask overlap area between the cell and its candidates. To correct for multiple assignments of a candidate, an inverse AHP approach was used in which the optimal cell from frame *k* was selected for the candidate of frame *k+1*. Finally, pairwise tracks over all timepoints were combined to form complete single cell trajectories. The code

for single-cell trajectory reconstruction was implemented in *bacto\_tracker/tracking.m*.

## Results

### Acquisition of high-resolution, large-scale, time course images of bacterial predation

The first step to develop and validate a method to perform single cell tracking within a complex bacterial community was to select and adapt an appropriate experimental assay. For this, we chose the predation of *E. coli* by *M. xanthus*, a well-established and well-adapted assay (Berleman *et al.*, 2006; Panigrahi *et al.*, 2021). We applied a few specific adaptations to this classical assay to limit the number of regions where cells cluster at extremely high-densities (e.g., colony edges) or form multi-layers. In our assay, a colony of *M. xanthus* was spotted at a millimeter distance from a colony of *E. coli* on a hard agar surface (Figure 1A) so that *M. xanthus* cells could reach the *E. coli* prey colony within a reasonable time period (~1–2 days). The optical density of *E. coli* was considerably reduced to prevent the formation of a sharp colony edge with high cell densities. In these conditions, *E. coli* grows in relatively small, intersped microcolonies typically 30µm wide with a single layer of cells (see Methods).

Acquisition of imaging data at relevant spatial and temporal scales requires a tradeoff between imaging areas large enough to capture collective cell displacements over long distances, and high imaging rates enabling the reconstruction of single cell trajectories over extended acquisitions. The imaging area provided by large-sensor sCMOS cameras (2048x2048 pixels) combined with a high magnification objective allowing for single-cell imaging (e.g., 60x) does not provide a sufficiently large area (0.05 mm<sup>2</sup>) to visualize events at scales relevant to the community. For instance, the area explored by *M. xanthus* cells ahead of the large collective cell groups (swarms) is ~0.05mm<sup>2</sup>, to track at the same time the movement of single cells and swarms requires considerably larger imaging areas. To increase the size of the region tracked, we constructed 3-by-3 mosaic images by acquiring and tiling neighboring fields-of-view (FOV). A serpentine pattern was used to minimize stage displacement between successive images (Figure 1B). An overlap of 200 pixels (17µm) was used to allow for efficient and robust reassembly of tiles into a single image of ~ 0.36 mm<sup>2</sup>. For each tile, brightfield and multiple fluorescence channels were imaged to enable the semantic segmentation of multiple bacterial species, and the subcellular localization of protein complexes.

To account for possible tilt in the sample or for agar pad deformation, 3D stacks spanning 3–4µm in the axial direction were acquired (7–9 planes, interspaced by 500nm). This allowed us to capture bacterial cells in-focus over a large FOV. An imaging cycle, corresponding to one time point in the timelapse, was completed when all z-stacks for each of the nine FOVs were acquired in both brightfield and fluorescence channels. Live axial drift correction based on the reflection of an infrared laser beam (785 nm) was used to maintain the focus during the course of the experiment (>6h). By

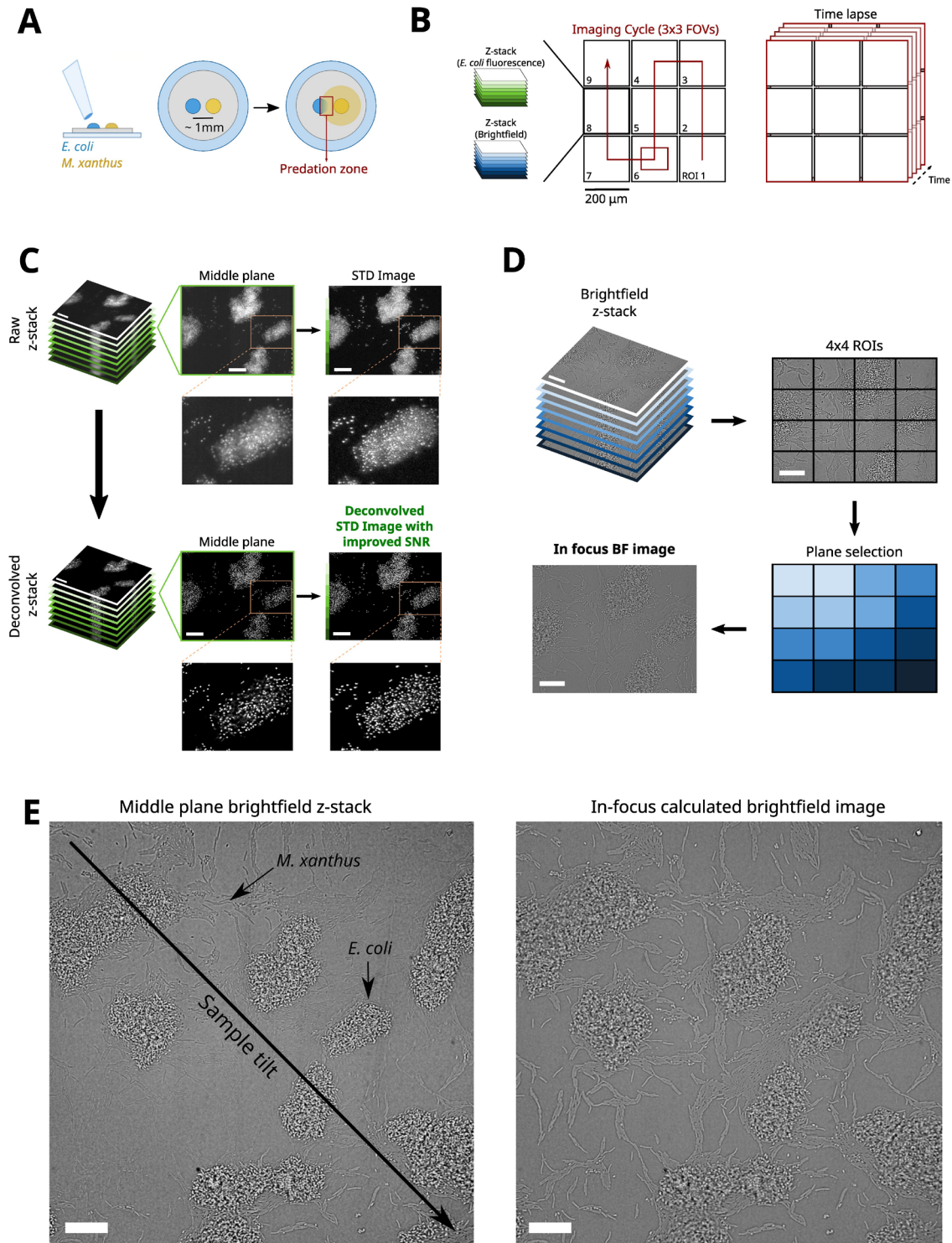


**Figure 1.** **A**) Sample preparation of a predation assay. A colony of *M. xanthus* (yellow) is spotted at a millimeter distance from a colony of *E. coli* (blue) on a hard agar surface. This sample is then incubated for 48-72 hours before imaging the forefront of the predation zone (red boxed area). **B**) Mosaic imaging of the predation forefront. The region of interest (ROI) is imaged by dividing it into a 3-by-3 mosaic made up of 2048x2048 pixels Field Of Views (FOVs). For each FOV at least two z-stacks are acquired, one for the *E. coli* fluorescence channel and one for the *E. coli* fluorescence channel. The acquisition of each mosaic FOV with its corresponding z-stacks acquired in a serpentine pattern makes up an imaging cycle. By repeating the acquisition of imaging cycles, a timelapse is constructed of the large ROI. **C**) Processing of *E. coli* fluorescence z-stacks to 2D images. The *E. coli* fluorescence z-stack is deconvolved and a 2D standard deviation image is calculated from the deconvolved z-stack to enhance the signal to noise ratio. Scalebars = 20  $\mu\text{m}$ . **D**) Processing of the brightfield z-stacks to 2D images. The brightfield z-stack is divided into 4x4 blocks, and for each block the in-focus plane is selected. A 2D in-focus brightfield image is reconstituted by retaining all selected planes. Scalebars = 20  $\mu\text{m}$ . **E**) In-focus calculation of brightfield images as a solution to sample tilt. Scalebars = 20  $\mu\text{m}$ .



repeating the 3-by-3 mosaic imaging cycle, a time lapse of a  $\sim 0.36\text{mm}^2$  area of the predation assay was acquired.

Robust and efficient reconstruction of single cell tracks requires a minimal overlap of cell masks between consecutive acquisitions. *E. coli* cells are mostly immobile and *M. xanthus* cells move on average at 2-4  $\mu\text{m}/\text{min}$  (Shi & Zusman, 1993) have a typical length of  $\sim 4\text{-}5\ \mu\text{m}$  (Patra *et al.*, 2016). Thus, to ensure a  $\sim 50\%$  area overlap between consecutive frames, the acquisition time for a full 3x3, 3D, two-color mosaic image needs to be  $\sim 35\text{s}$  or smaller. To achieve this imaging time, we developed a fully-automated imaging routine written in LabView which synchronizes all the required hardware components: lasers, camera, piezo-electric z-stage, translation stage, field-programmable gate array (FPGA), and an autofocus system (see *Microscopy* section in Methods) (Cardozo Gizzi *et al.*, 2019).

Finally, newly acquired stacks are pre-processed to improve the signal to noise ratio, and project the 3D image stack into a single in-focus 2D image. For the fluorescence channel, 3D-stacks were first deconvolved (see *Treatment of fast time lapse data* in Methods) and a 2D image was then calculated by computing the standard deviation projection of the deconvolved stack (Figure 1C). For the brightfield channel, in-focus 2D images were reconstructed in three steps (Figure 1D). First, the brightfield 3D-stack was subdivided into 16 blocks of 512x512 pixels. For each image of the blocks, the modulation transfer function was calculated by computing the line spread function along the x and y directions. The images with the sharpest features were then selected from each block and recombined into a single 2048x2048 in-focus image (Figure 1E).

### AI-based semantic cell segmentation

To segment cells semantically, we developed a deep learning approach. This approach was based on a convolutional neural network (CNN) with a U-net architecture provided by Matlab R2019 (Ronneberger *et al.*, 2015). The inputs of the network were an in-focus 2D bright-field image containing both *M. xanthus* and *E. coli* cells and a 2D standard deviation fluorescence image of fluorescently-labeled *E. coli*. For the U-net training, an image database was created and contained representative data from different experimental conditions, including images with either low or high *M. xanthus* cell densities (such as in swarms), small *E. coli* colonies, and both bacterial species in close spatial proximity or intermixed (Figure 2A). In total, forty 260-by-260 pixels images, composed of one brightfield image and the associated fluorescence image of *E. coli* nucleoid (HU-mCherry), were manually annotated using five distinct classes: i) background, ii) *M. xanthus* body, iii) *M. xanthus* contour, iv) *E. coli* body, and v) *E. coli* contour (Figure 2B). The contour of cells in densely packed regions was allowed to overlap and was included as a distinct class as this forced the network to spatially separate single cell bodies. From each annotated 260-by-260 pixels image, several 128-by-128 pixels training images were sampled. The training dataset was further expanded by calculating the annotated 45°-rotated 182-by-182 pixels image and sampling

several training images from these calculated images. This allowed us to omit the time-consuming and labor intensive process of manually annotating numerous experimental images. To increase the robustness of the semantic segmentation slightly out-of-focus images were included for each image in the training dataset (Shorten & Khoshgoftaar, 2019). Finally, a classical data augmentation step was performed, including for example left-right and up-down flipping of the training images. Note that automatic rotation was not allowed for data augmentation during training since it often created mis-labeling errors (contour vs. body) when working with densely packed cells images. Finally, each pair of raw/labeled images were randomly assigned to either a training set (70% of the data), a validation set (15%) or a testing set (15%). Training was performed using a U-net architecture composed of an encoder-decoder depth of 3, filter size of 5x5x2, and allowing image augmentation (random up-down, left-right flip).

The performance of the trained network, defined by the ability of a network to accurately classify a pixel, was evaluated by calculating the confusion matrix from the testing set (Figure 2C). The confusion matrix represents how well the network predicts the class of a given pixel using the ground truths of the testing set. The diagonal of the confusion matrix indicates how often the network properly predicts a class: for instance, 87% of the pixels annotated as *M. xanthus* cell body in the ground truth are predicted as *M. xanthus* cell body by the network. The non-diagonal terms indicate errors: for example, 1.142% of the *M. xanthus* cell body pixels are improperly assigned to *E. coli* cell body. Using this analysis, we observe that the trained network is able to efficiently differentiate *M. xanthus* from *E. coli* cells with  $>87\%$  accuracy. The assignment of the *M. xanthus* and *E. coli* contour classes were often intermixed with the respective cell body class or the background. However, this did not pose a problem *per se*, as the classes for cell contour were only used to properly separate cell body masks in regions where cells were densely packed, and these improper pixel assignments are filtered out by filtering steps (see below).

Robust construction of single-cell trajectories from masks segmented at different time points could be compromised when cell masks in close physical proximity are not properly separated and merge into one large mask. To avoid this bias, we adopted a strategy in which five networks were independently trained (Figure 2D). Each network used a refocused 2D brightfield image and its corresponding 2D deconvolved fluorescence image as inputs and outputs the corresponding segmented image. Therefore, from the five networks, five slightly different segmentations are obtained, respectively for *E. coli* and *M. xanthus* cells. These images are combined into a probabilistic image with a confidence value ranging between 0 and 5 for the assignment of each pixel to either the class of *E. coli* or the class of *M. xanthus*, with 0 being the case where none of the five networks assigned the pixel to a given class and 5 being the case where all five networks assigned the pixel to a given class (Figure 2E). This strategy allowed us to perform a stringent segmentation of each single cell and to converge to an accurate result for which limited

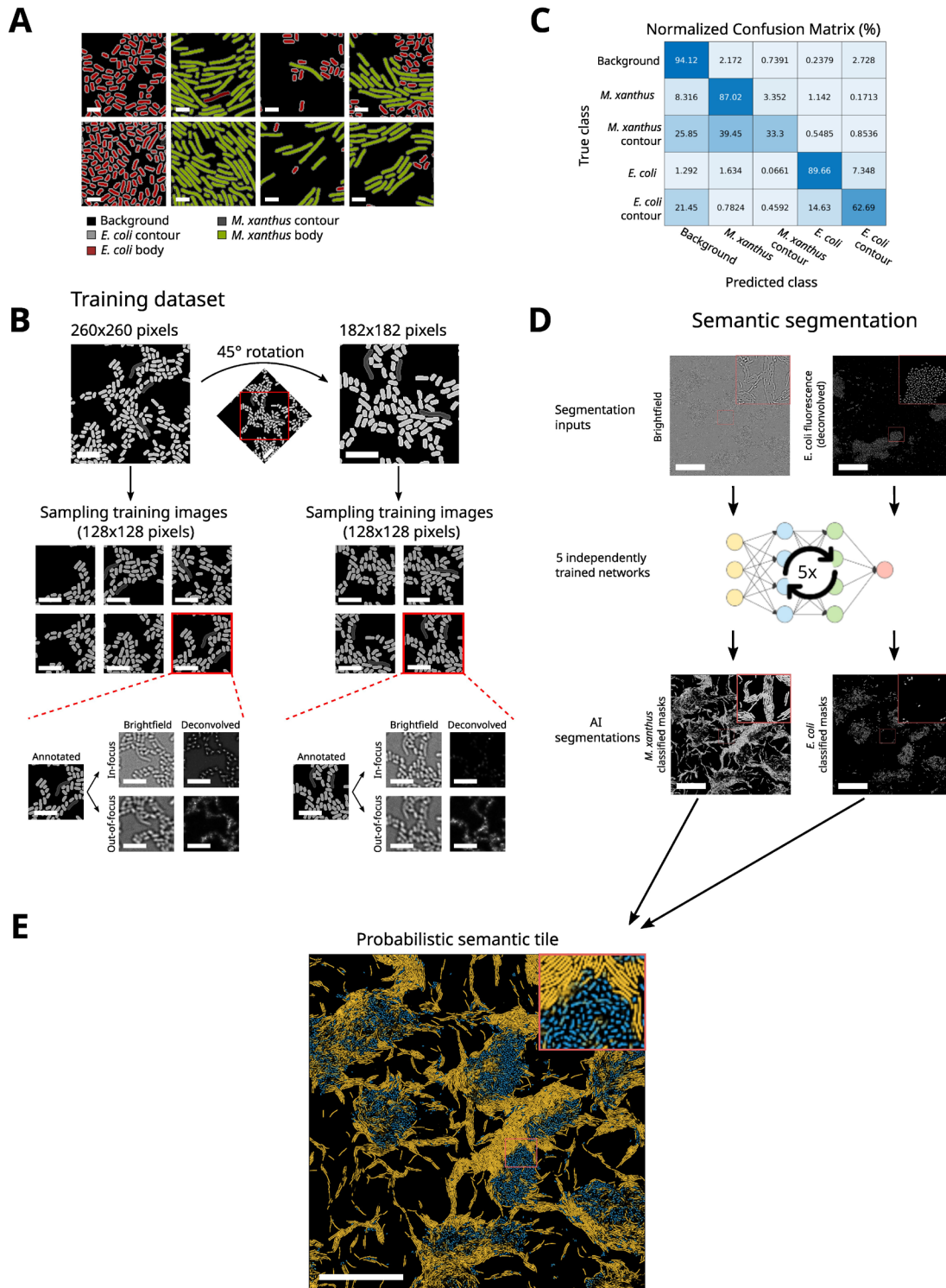


**Figure 2. Semantic segmentation with MATLAB-based U-net algorithm.** **A**) Example of ground truth images. Images are annotated for the five classes: i) background, ii) *E. coli* body, iii) *E. coli* contour, iv) *M. xanthus* body, and v) *M. xanthus* contour. Scalebars = 2  $\mu$ m. **B**) Example of an annotated image for the set-up of the training image database. From a 260x260 pixel image annotated for the ground truth, a number of training images (128x128 pixels) were sampled. For each sampled training image, several out-of-focus brightfield and fluorescence images were included as well. The 260x260 pixels image was then 45° rotated from which additional training images were sampled. Out-of-focus brightfield and fluorescence images were included again. Scalebars = 5  $\mu$ m. **C**) Normalized Confusion Matrix for a trained U-net. From this matrix, the accuracy of pixel assignment to a given class predicted by the trained network is evaluated by comparing it to the ground truth. **D**) Semantic segmentation of experimental input images. The inputs for the U-net are brightfield and fluorescence images. Segmentation is performed by five independently trained networks that output an image containing the confidence value for each pixel for each class. Scalebars = 50  $\mu$ m. **E**) A probabilistic semantic tile can be assembled visualizing the *E. coli* (blue) and *M. xanthus* (yellow) body classes. Scalebar = 50  $\mu$ m.

post-processing of the segmented masks was required for further analysis.

### Reconstruction and registration of large-scale tiled images

Next, we developed a method to assemble the 3-by-3 mosaics, acquired every 35s into single images. For this, we used an iterative image cross-correlation algorithm that determines the overlap between any two neighboring images with pixel precision. To ensure smooth transitions between tiles in the final image, we combined tiles using an alpha blending method with a decreasing transparency gradient (Figure 3A). A typical acquisition that captures *M. xanthus* predation requires the imaging of the same region for extended time periods (~6h), during which the microscope stage drifts laterally mainly due to temperature variations. To account for lateral drift, we performed image registration for all time-points by cross-correlating assembled images of the *E. coli* segmented image with the reference image from the first time-point (Figure 3A).

Finally, probabilistic *M. xanthus* masks were converted to binary masks by applying several filtering steps (Figure 3B). These steps were included to resolve occasional merged masks and ensure that only true single-cell masks were included for the single-cell tracking of *M. xanthus* cells. First, we filtered pixels with high confidence values. For each mask, pixels in the perimeter with lower confidence values are retained only when the mask area does not increase more than 5% to avoid fusing neighboring cell masks. The output of this pixel selection procedure is a binary image with 4-connected *M. xanthus* cell masks. Second, *M. xanthus* masks with areas lower than 100 pixels were rejected to reinforce semantic segmentations, as typical *M. xanthus* cells contained several hundred pixels. An additional filtering, based on branchpoint detection and tortuosity, was applied to reject fused cell masks which could not be detected in the pixel selection step (Figure 3B). As *M. xanthus* are rod-shaped cells, their backbone is a line without any branchpoints. Pole-to-body mask fusions can thus be detected and rejected by calculating the backbone of all masks and identifying branch points (Figure 3B, green boxed area). Furthermore, pole-to-pole mask fusions for which no branchpoint could be calculated were detected by calculating the tortuosity, which is a measure of curvature, of the mask defined as the ratio between the length of the backbone and the distance between the endpoints of the backbone. The mask was rejected when the tortuosity exceeded the threshold of two (Figure 3B, red boxed area). The masks retained after these post-processing steps were used to construct the final assembled images and to reconstruct single-cell trajectories, as described in the next section (Figure 3C).

### Single-cell tracking

The construction of single-cell *M. xanthus* trajectories requires robust algorithms that link together masks from the same cell acquired at different time points. A method that relies exclusively on the maximization of overlap between cell

masks at consecutive time points works well for isolated cells, but not in more challenging conditions where cells are densely packed in space (e.g., swarms). To deal with cells in these dense regions, we developed an analysis method that uses, in addition to the overlap of masks between consecutive time points, multiple morphological mask parameters and a ranking approach.

Specifically, this approach consists of three distinct stages: i) pairwise tracking, ii) filtering of pairwise tracks, and iii) track reconstruction. In the first stage, we connected pairs of masks detected in consecutive time frames by constructing, for each mask at time  $t$ , the list of candidate masks at time  $t+1$ . Candidates were selected by finding the masks at time  $t+1$  that partially overlapped with the dilated bounding box of the cell of interest at time  $t$ . Three scenarios were frequent: (i) no candidate was found, making it impossible to make a pairwise connection between the cell of interest and its candidate; (ii) a unique suitable candidate was found, a typical scenario for isolated cells, allowing a straightforward pairwise connection between the masks at times  $t$  and  $t+1$ ; and (iii) multiple candidates were found, a typical case for groups of cells, making several pairwise connections possible. When multiple candidates were found, we calculated the cell length, the mask area and their overlap for the cell of interest and for the candidates. These parameters were used as inputs for Analytical Hierarchy Processing (AHP), a method that ranks all the possible pairwise associations from most to least likely (Saaty, 1986) and thus, allowed us to select the most likely pairwise association (Figure 4A). The process of candidate selection and pairwise association was iteratively repeated for all cell masks at time  $t$ .

For cells in densely packed regions, multiple assignments of the same candidate at time  $t+1$  could occur, indicating that the same candidate at time  $t+1$  was selected for pairwise association with two or more cells of interest at time  $t$  (Figure 4B). To resolve such conflicts, we implemented a filtering step in which these multiple assignments were detected and retained. Then, to connect the correct pair of masks, a reverse strategy was used in which the mask at time  $t+1$  became the cell to track and the masks at time  $t$  became the candidates. Similarly, as before, the parameters for cell length, mask area and overlap were used as inputs for the AHP, allowing us to rank the pairwise associations and select the most likely connection. This filtering step finally results in a list of unique pairwise connections, essential for more robust track reconstruction.

After reconstructing and filtering the pairwise associations for all sets of consecutive images, full-length tracks were assembled by iteratively connecting cell IDs from pairwise tracks (Figure 4C). We note that while this methodology considerably improves the robustness of track reconstruction, it still has limitations. A specific limitation is its ability to track *M. xanthus* cells within regions containing multiple cell layers, for instance within *E. coli* islands or in extremely large swarms. In these cases, our algorithm selects and analyzes the



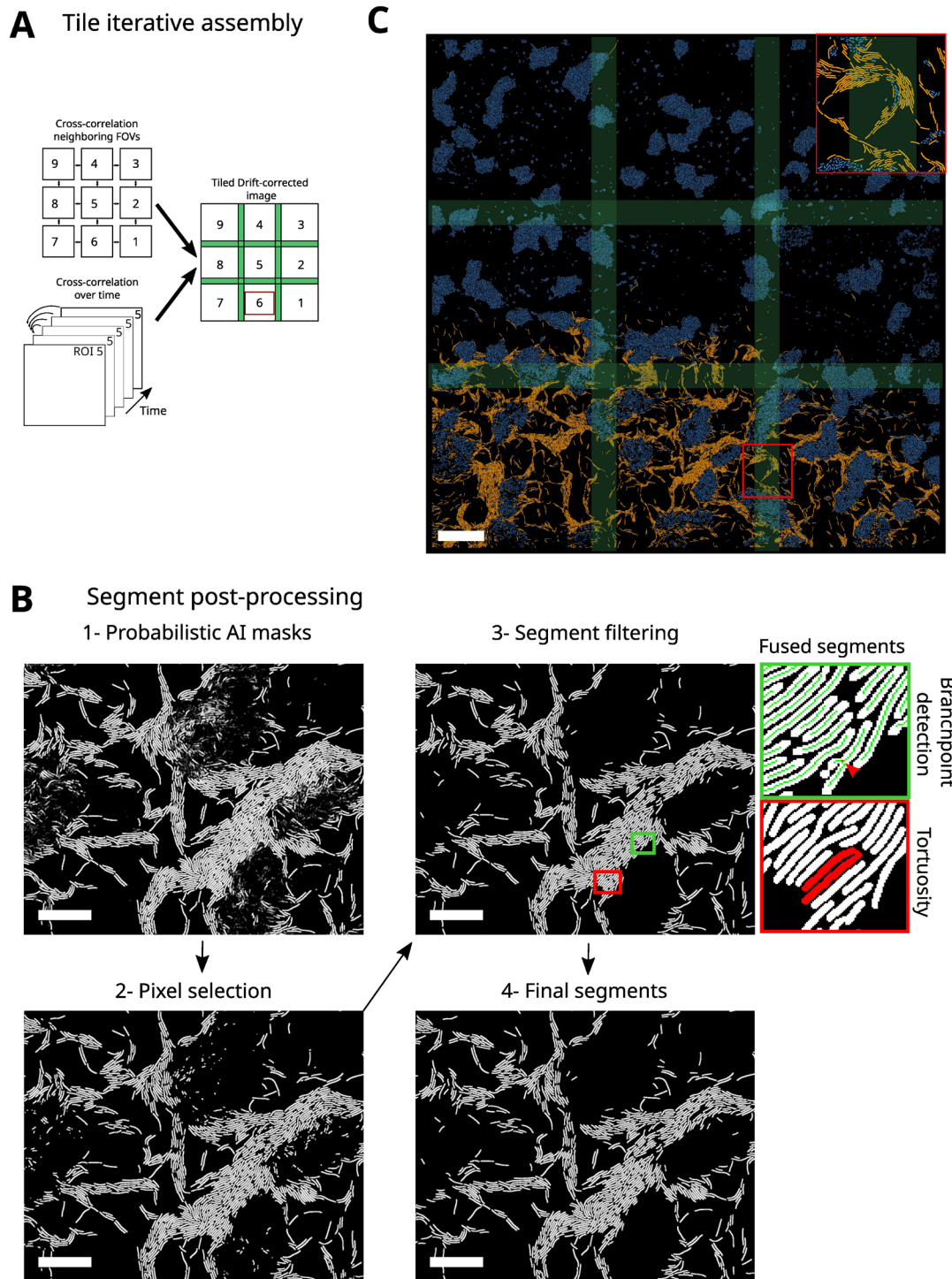


**Figure 3. Image post-processing.** **A**) Image post-processing to reassemble a large ROI and to correct drift. By calculating the cross correlation of the overlap region (green area in the final processed image) between neighboring FOVs, their corresponding pixel-precise positioning in the mosaic can be determined. After the tiling of the mosaic, a drift correction is applied based on the cross-correlation between the middle FOV at time  $t$  with the middle reference FOV reference at time  $t=1$ . **B**) Post-processing of the segments to reject all improper masks. Raw probabilistic *M. xanthus* AI masks are first converted to a binary image by selecting pixels based on their confidence values (1), masks are then filtered for size and finally fused masks are rejected based on backbone branch points (green boxed area) and tortuosity (red boxed area) (2). Scalebars= 20  $\mu\text{m}$ . **C**) Final assembled, drift-corrected, and post-processed semantic masks of *M. xanthus* (yellow) and *E. coli* (blue). Scalebar = 50  $\mu\text{m}$ .



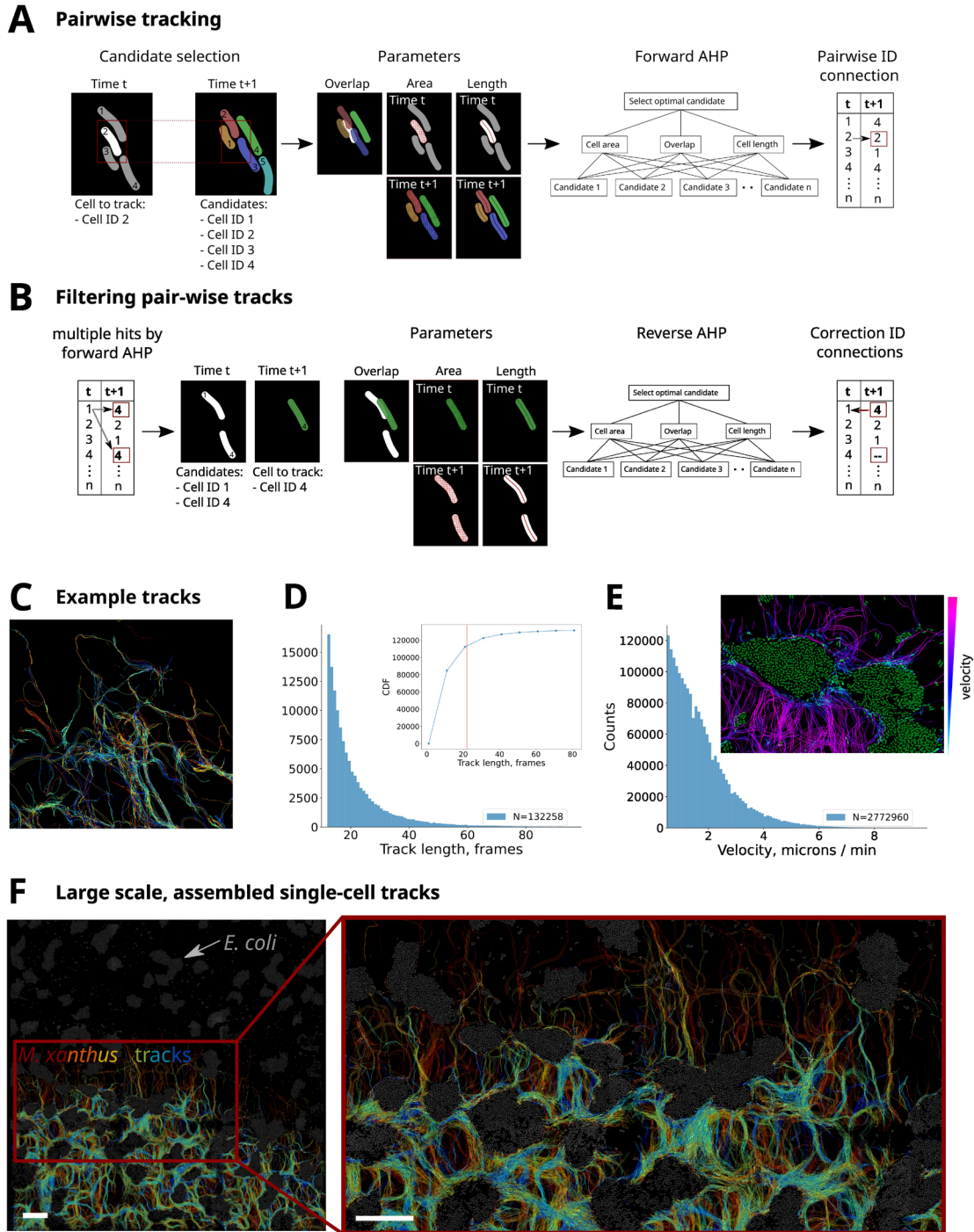


**Figure 4. Schematic of single-cell tracking method.** **A**) Pairwise tracking to connect all masks at time  $t$  to their corresponding masks at time  $t+1$ . For each mask at a given time point (time  $t$ ), candidate masks for connection are selected in the consecutive time point (time  $t+1$ ) based on the bounding box of the mask ( $t$ ). For the mask ( $t$ ) and candidates ( $t+1$ ), three parameters are calculated: i) the cell length based on its backbone, ii) the cell area and the overlap between the mask ( $t$ ) and iii) the mask of the candidate ( $t+1$ ). These parameters are the input for the Analytical Hierarchy Processing (AHP) which ranks the candidates from most suitable to least suitable for connection. This process is repeated for all masks ( $t$ ) and results in a list of pairwise connections. **B**) Filtering and correction of multiple assignments in pairwise connection lists. To account for multiple assignments of a candidate, a reverse AHP step is included in which the most suitable mask ( $t$ ) is selected for the candidate ( $t+1$ ). The list of pairwise connections is then corrected, for masks ( $t$ ) that were not selected in the reverse AHP, the trajectory is stopped. **C**) Selection of single *M. xanthus* tracks color-coded by track identity in a region of interest of  $115\mu\text{m}$ . Only a small number of tracks are represented ( $N = 383$ ) for clarity. **D**) Histogram of track lengths for the full dataset. Inset displays the cumulative distribution function. Red line indicates the mean track length.  $N = 132258$  indicates the number of tracks. **E**) Histogram of track instant velocities ( $N = 2772960$  tracks). Inset: region of the 3-by-3 mosaic where *E. coli* masks are shown in green and *M. xanthus* tracks are displayed according to their velocity (see colormap on the right). **F**) Example of reconstructed tracks in a 3-by-3 mosaic for a full experiment (700 time points). *E. coli* cells are shown in gray. *M. xanthus* tracks are color-coded by time. Scalebars =  $50\mu\text{m}$ .

focal plane where most cells are in-focus, thus missing in the process out-of-focus cells whose tracks cannot be properly completed. We envision that development of 3D AI segmentation methods will be necessary to bypass this limitation.

Time-lapse experiments in 3x3 mosaics covering  $\sim 0.36 \text{ mm}^2$  at 35s time resolution were used to obtain full-length single cell trajectories. An example of the final tracks can be visualized in the Extended Data 1. These trajectories can be used to characterize the tracking process, for example through the track length distribution (Figure 4D). On average, cells were tracked for  $\sim 22$  frames = 768s. The ability of our algorithm to reconstruct longer tracks was limited by cells leaving the imaging area, and by the tracking of out-of-focus cells (see above), or within extremely high-density areas where our reconnection approaches were unable to converge to a unique solution or when masks were filtered out due to segmentation errors (see Figure 3B). Despite these limitations, the high-throughput of our method enabled the reconstruction of thousands of long tracks:  $>19,000$  tracks more than  $\sim 770$ s-long.

In addition to track lengths, single-cell trajectories can be used to calculate dynamic properties, such as the distribution of instant speeds (Figure 4E). The measured speeds are consistent with speeds previously reported in the literature (2-4  $\mu\text{m}/\text{min}$ ) (Shi & Zusman, 1993). We note that an interesting feature of our approach is that track properties (such as speed) can be used to detect spatial changes in single cell dynamic behaviors. For instance, by embedding speed into cell masks we observe that *M. xanthus* cells have the tendency to slow down when they reach *E. coli* islands (Figure 4E, inset).

Finally, representation and analysis of thousands of tracks over mm-scales permits the monitoring of large-scale single-cell dynamics over biologically-relevant timescales (Figure 4F), such as migration of *M. xanthus* between *E. coli* islands during predation.

## Discussion

In this article, we propose an imaging, cell segmentation and tracking framework for the study of predation of *M. xanthus* on *E. coli*. Our high-throughput, high resolution microscopy method allows the acquisition of large imaging areas in a timelapse manner by employing a mosaic imaging scheme. We propose a deep learning-based semantic segmentation approach for the reconstruction of single-cell *M. xanthus* and *E. coli* masks. And finally, we present a method that enables the tracking of motile *M. xanthus* cells.

The workflow proposed here allowed us to overcome several challenges for capturing single-cell dynamics of complex multicellular systems. First, mosaic imaging allows the visualization of extensive areas without sacrificing resolution and thus, thousands of single-cells can be tracked together with their position within the community to provide spatial context. Mosaic approaches are widely used for the imaging of fixed biological specimens, such as tissue slices (Chow

*et al.*, 2006; Price *et al.*, 2006) and are often incorporated in commercial microscopes. However, we found that their adaptation to dynamic imaging requires certain tradeoffs, particularly constraining when multi-color, multimodal, and multi-plane acquisitions are required. Specifically, the maximum imaging area scales linearly with the acquisition time per mosaic ( $\sim 35$ s, in our case defined by the time needed for a cell to travel half its length). This relation implies that increases in the imaging area can be achieved by shortening the time required for the acquisition of a single tile, or by slowing the system dynamics (i.e., cell speed). The robotic microscope we implemented enabled the acquisition of 3x3 tiles at frame rates able to capture the relevant biological timescales in our predation assay. We note that further reduction of the acquisition time could be achieved by resorting to multi-focus systems using multiple cameras to acquire several planes at once (Chao *et al.*, 2017), or by removing the need to acquire multi-modal, multi-focus datasets. Alternatively, remote refocusing techniques (Botcherby *et al.*, 2008) which are becoming increasingly popular for rapid, 4D optical imaging ([https://andrewgyork.github.io/remote\\_refocus/appendix.html](https://andrewgyork.github.io/remote_refocus/appendix.html)) would considerably reduce the acquisition time of single volumes. We envision that the use of oblique-plane microscopes could also contribute in future to the high-resolution acquisition of large complex samples, such as biofilms, with reduced acquisition times (Sapoznik *et al.*, 2020).

An important challenge arising from the acquisition method we developed is the handling, analysis and storage of large numbers of images ( $\sim 1000$  3D, multi-channel volumes per experiment). We solved this challenge by resorting to automatic, robust image analysis tools that required minimal user input. For this, we used a deep learning method based on the U-net architecture, similar to our recent development (Panigrahi *et al.*, 2021), to segment and identify multiple species in millimeter-sized 2D images. The field of image analysis using deep-learning is moving fast (Greener *et al.*, 2021; Hallou *et al.*, 2021) and more robust, and flexible possibilities are likely to emerge in future. For instance, the use of 3D AI-based segmentation will likely be capable of semantically segmenting bacterial cells within multi-layered samples, such as biofilms (Weigert *et al.*, 2020; Zhang *et al.*, 2020), thus enabling the tracking of cells in multi-layers.

Finally, we implemented an algorithm to reconstruct single-cell trajectories of motile *M. xanthus* cells from single cell masks. By using a ranking approach for complex decision making (Saaty, 1986), we were able to improve the tracking of cells in different environments, including cells in isolation, in small groups, and in larger swarms. Other bacterial cell segmentation algorithms were developed in the past for the tracking of bacterial cells at low densities, in mother-machines, or for lineage tracing (reviewed in (Jeckel & Drescher, 2021)). However, these methods are either ill-adapted for robust, automatic analysis required of high-throughput tracking datasets, for semantic detection of different species, or for single-cell tracking within complex communities displaying high cell densities. More recently, a new approach using

deep-learning to retrieve single-cell tracks for lineage tracking was developed (O'Connor *et al.*, 2022). However, this development does not perform semantic segmentation, and it is unclear how it will perform on bacteria with curved shapes (such as *M. xanthus*), or in samples with large number of cells, high cell densities, or with multi-layers. A main challenge ahead will be to improve the efficiency of detection, 3D segmentation and tracking of single cells within densely packed multilayers, such as those encountered in biofilms. Taken together, this workflow opens the door for the quantitative study of bacterial predation of *M. xanthus* on *E. coli*. In addition, we predict that this workflow should be easily used to study other complex and multispecies systems.

## Conclusion

In this paper, we presented several methods for the acquisition and analysis of the dynamics of single bacterial cells within complex micro-environments. For this, we developed a hardware-accelerated, automated microscope to robustly image large areas of the sample, over long periods of time, and with high temporal resolution. Next, we applied a UNET-based, deep-learning approach to semantically segment single bacterial cells within densely-packed cell groups. Third, we designed a cell tracking algorithm to track single motile cells. Finally, we applied these technologies to the predation of *E. coli* by *M. xanthus* and extracted dynamic track parameters from thousands of single-cell tracks with spatial resolution. In this paper, we presented several methods for the acquisition and analysis of the dynamics of single bacterial cells within complex micro-environments. For this, we developed a hardware-accelerated, automated microscope to robustly image large areas of the sample, over long periods of time, and with high temporal resolution. Next, we applied a UNET-based, deep-learning approach to semantically segment single bacterial cells within densely-packed cell groups (Nollmann, 2022c). Third, we designed a cell tracking algorithm to track single motile cells. Finally, we applied these technologies to the predation of *E. coli* by *M. xanthus*, and extracted dynamic track parameters from thousands of single-cell tracks with spatial resolution.

## Data availability

### Underlying data

Open Science Framework: bacto\_tracker/Underlying Data Tables. <https://doi.org/10.17605/OSF.IO/3WKVN>. (Nollmann, 2022a).

The project contains the following underlying data:

- Underlying Data Tables.docx. (Tables for strains used in bacto\_tracker and for a step-by-step data processing description).

Underlying Data are available under the terms of the Creative Commons Zero “No rights reserved” data waiver (CC0 1.0 Public domain dedication).

## Validation images and tracks

Open Science Framework: Images, tracks and segmentations using bacto\_tracker. <https://doi.org/10.17605/OSF.IO/NZSEF>. (Nollmann, 2022b).

This project contains the following files:

- data.zip. (This file contains a folder (“data”) with a single file (“track\_TXY.csv”) and three sub-folders: example\_image, masks, and Track\_IDs. The example\_images folder contains raw TIF images of Ch1 (fluorescence signal of *E.coli*) and Ch2 (bright field image of *Myxococcus xanthus* and *E. coli*). Due to size limitations, only the 10 first frames for ROI number nine are provided in this dataset. These, however, can be used to apply bacto\_tracker to segment masks of *E. coli* and *M. xanthus*, as well as for building trajectories. The masks folder contains the masks of *M. xanthus* extracted for each frame and each ROI of the full experiment. Please refer to Underlying Table 2 for more information. The Track\_IDs folder contains the tracks extracted for the full experiment. Please refer to Underlying Table 2 for more information. Finally, the track\_TXY.csv file contains the result of applying create\_csv\_tracks.py. This file contains the full list of tracks extracted from this experiment.)

These datasets are available under the terms of the Creative Commons Zero “No rights reserved” data waiver (CC0 1.0 Public domain dedication).

## UNET networks

Open Science Framework: UNET networks. <https://doi.org/10.17605/OSF.IO/TFMVY>. (Nollmann, 2022c).

This project contains the following files:

- Trained\_network\_1\_20\_Mar\_2020.mat
- Trained\_network\_2\_20\_Mar\_2020.mat
- Trained\_network\_3\_13\_Mar\_2020.mat
- Trained\_network\_4\_13\_Mar\_2020.mat
- Trained\_network\_5\_20\_Mar\_2020.mat

These networks are available under the terms of the Creative Commons Zero “No rights reserved” data waiver (CC0 1.0 Public domain dedication).

## Extended data

Open Science Framework: Single-cell Tracking Video. <https://doi.org/10.17605/OSF.IO/VE3SC>. (Nollmann, 2022d).

This project contains the following extended data:

- Supp\_Video\_1.mp4. (Extended Data 1: Example tracks of *M. xanthus* within a field of *E. coli* microcolonies. *E. coli* masks are shown in green for the first frame)



of the movie and in red for the final frame. *M. xanthus* masks are shown in pink. White circle represents the centroid of the cell at different time points. Only a small selection of tracks are represented for clarity.)

Extended Data are available under the terms of the Creative Commons Zero “No rights reserved” data waiver (CC0 1.0 Public domain dedication).

## Software availability

Source code available from: [https://github.com/NollmannLab/bacto\\_tracker](https://github.com/NollmannLab/bacto_tracker)

Archived source code at time of publication: <https://doi.org/10.17605/OSF.IO/JQDWE>.

License: CCO 1.0 Universal.

## References

- Berleman JE, Chumley T, Cheung P, et al.: **Rippling Is a Predatory Behavior in *Myxococcus Xanthus***. *J Bacteriol*. 2006; **188**(16): 5888–95.  
[PubMed Abstract](#) | [Publisher Full Text](#) | [Free Full Text](#)
- Botcherby EJ, Juškaitis R, Booth MJ, et al.: **An Optical Technique for Remote Focusing in Microscopy**. *Optics Communications*. 2008; **281**(4): 880–87.  
[Publisher Full Text](#)
- Bustamante VH, Martínez-Flores I, Vlamakis HC, et al.: **Analysis of the Frz Signal Transduction System of *Myxococcus Xanthus* Shows the Importance of the Conserved C-Terminal Region of the Cytoplasmic Chemoreceptor FrzCD in Sensing Signals**. *Mol Microbiol*. 2004; **53**(5): 1501–1513.  
[Publisher Full Text](#)
- Cardozo Gizzi AM, Cattoni DI, Fiche JB, et al.: **Microscopy-Based Chromosome Conformation Capture Enables Simultaneous Visualization of Genome Organization and Transcription in Intact Organisms**. *Mol Cell*. 2019; **74**(1): 212–22.e5.  
[PubMed Abstract](#) | [Publisher Full Text](#)
- Chao J, Velmurugan R, You S, et al.: **Remote Focusing Multifocal Plane Microscopy for the Imaging of 3D Single Molecule Dynamics with Cellular Context**. *Proc SPIE Int Soc Opt Eng*. 2017; **10070**: 100700L.  
[PubMed Abstract](#) | [Publisher Full Text](#) | [Free Full Text](#)
- Chow SK, Hakozaki H, Price DL, et al.: **Automated Microscopy System for Mosaic Acquisition and Processing**. *J Microsc*. 2006; **222**(Pt 2): 76–84.  
[PubMed Abstract](#) | [Publisher Full Text](#)
- Devi S, Alexandre YO, Loi JK, et al.: **Adrenergic Regulation of the Vasculature Impairs Leukocyte Interstitial Migration and Suppresses Immune Responses**. *Immunity*. 2021; **54**(6): 1219–30.e7.  
[PubMed Abstract](#) | [Publisher Full Text](#)
- Ducret A, Quardokus EM, Brun YV: **Microbej, a Tool for High Throughput Bacterial Cell Detection and Quantitative Analysis**. *Nat Microbiol*. 2016; **1**(7): 16077.  
[PubMed Abstract](#) | [Publisher Full Text](#) | [Free Full Text](#)
- Dworkin M: **Nutritional Regulation of Morphogenesis in *Myxococcus Xanthus***. *J Bacteriol*. 1963; **86**(1): 67–72.  
[PubMed Abstract](#) | [Publisher Full Text](#) | [Free Full Text](#)
- Greener JG, Kandathil SM, Moffat L, et al.: **A Guide to Machine Learning for Biologists**. *Nat Rev Mol Cell Biol*. 2021; **23**(1): 40–55.  
[PubMed Abstract](#) | [Publisher Full Text](#)
- Hallou A, Yevick HG, Dumitrascu B, et al.: **Deep Learning for Bioimage Analysis in Developmental Biology**. *Development*. 2021; **148**(18): dev199616.  
[PubMed Abstract](#) | [Publisher Full Text](#) | [Free Full Text](#)
- Jacobson A, Yang D, Vella M, et al.: **The Intestinal Neuro-Immune Axis: Crosstalk between Neurons, Immune Cells, and Microbes**. *Mucosal Immunol*. 2021; **14**(3): 555–65.  
[PubMed Abstract](#) | [Publisher Full Text](#) | [Free Full Text](#)
- Jeckel H, Drescher K: **Advances and Opportunities in Image Analysis of Bacterial Cells and Communities**. *FEMS Microbiol Rev*. 2021; **45**(4): fuaa062.  
[PubMed Abstract](#) | [Publisher Full Text](#) | [Free Full Text](#)
- Keane R, Berleman J: **The Predatory Life Cycle of *Myxococcus Xanthus***. *Microbiology (Reading)*. 2016; **162**(1): 1–11.  
[PubMed Abstract](#) | [Publisher Full Text](#)
- Muñoz-Dorado J, Marcos-Torres FJ, García-Bravo E, et al.: **Myxobacteria: Moving, Killing, Feeding, and Surviving Together**. *Front Microbiol*. 2016; **7**: 781.  
[PubMed Abstract](#) | [Publisher Full Text](#) | [Free Full Text](#)
- Nauseef WM, Borregaard N: **Neutrophils at Work**. *Nat Immunol*. 2014; **15**(7): 602–11.  
[PubMed Abstract](#) | [Publisher Full Text](#)
- Nollmann M: **Underlying Data Tables**. Dataset. 2022a.  
<http://www.doi.org/10.17605/OSF.IO/3WKVN>
- Nollmann M: **Images, tracks and segmentations using bacto\_tracker**. Dataset. 2022b.  
<http://www.doi.org/10.17605/OSF.IO/NZSEF>
- Nollmann M: **UNET networks**. Dataset. 2022c.  
<http://www.doi.org/10.17605/OSF.IO/TFMYY>
- Nollmann M: **Single-cell tracking video**. Dataset. 2022d.  
<http://www.doi.org/10.17605/OSF.IO/VE3SC>
- O'Connor OM, Alnahhas RN, Lugagne JB, et al.: **DeLTA 2.0: A Deep Learning Pipeline for Quantifying Single-Cell Spatial and Temporal Dynamics**. *PLoS Comput Biol*. 2022; **18**(1): e1009797.  
[PubMed Abstract](#) | [Publisher Full Text](#) | [Free Full Text](#)
- Paintdakhi A, Parry B, Campos M, et al.: **Oufiti: An Integrated Software Package for High-Accuracy, High-Throughput Quantitative Microscopy Analysis**. *Mol Microbiol*. 2016; **99**(4): 767–77.  
[PubMed Abstract](#) | [Publisher Full Text](#) | [Free Full Text](#)
- Panigrahi S, Murat D, Le Gall A, et al.: **MiSiC, a General Deep Learning-Based Method for the High-Throughput Cell Segmentation of Complex Bacterial Communities**. *Elife*. 2021; **10**: e65151.  
[PubMed Abstract](#) | [Publisher Full Text](#) | [Free Full Text](#)
- Patra P, Kissoon K, Cornejo I, et al.: **Colony Expansion of Socially Motile *Myxococcus Xanthus* Cells Is Driven by Growth, Motility, and Exopolysaccharide Production**. *PLoS Comput Biol*. 2016; **12**(6): e1005010.  
[PubMed Abstract](#) | [Publisher Full Text](#) | [Free Full Text](#)
- Price DL, Chow SK, Maclean NAB, et al.: **High-Resolution Large-Scale Mosaic Imaging Using Multiphoton Microscopy to Characterize Transgenic Mouse Models of Human Neurological Disorders**. *Neuroinformatics*. 2006; **4**(1): 65–80.  
[PubMed Abstract](#) | [Publisher Full Text](#)
- Rombouts S: **Advanced microscopies for the study of motility behavior in predating *Myxococcus xanthus***. Bacteriology. Université Montpellier, English. ffnnt: 2021MONTT084ff. fftel03637407f. 2021.  
[Reference Source](#)
- Ronneberger O, Fischer P, Brox T: **U-Net: Convolutional Networks for Biomedical Image Segmentation**. In: *Med Comput Vis (2015)*. Springer International Publishing. 2015; 234–41.  
[Publisher Full Text](#)
- Saaty TL: **Absolute and Relative Measurement with the AHP. The Most Livable Cities in the United States**. *Socioecon Plann Sci*. 1986; **20**(6): 327–31.  
[Publisher Full Text](#)
- Sapoznik E, Chang BJ, Huh J, et al.: **A Versatile Oblique Plane Microscope for Large-Scale and High-Resolution Imaging of Subcellular Dynamics**. *Elife*. 2020; **9**: e57681.  
[PubMed Abstract](#) | [Publisher Full Text](#) | [Free Full Text](#)
- Seef S, Herrouj, de Boissier P, et al.: **A Tad-like Apparatus Is Required for Contact-Dependent Prey Killing in Predatory Social Bacteria**. *Elife*. 2021; **10**: e72409.  
[PubMed Abstract](#) | [Publisher Full Text](#) | [Free Full Text](#)
- Shi W, Zusman DR: **The Two Motility Systems of *Myxococcus Xanthus* Show Different Selective Advantages on Various Surfaces**. *Proc Natl Acad Sci U S A*. 1993; **90**(8): 3378–82.  
[PubMed Abstract](#) | [Publisher Full Text](#) | [Free Full Text](#)
- Shorten C, Khoshgoufar TM: **A Survey on Image Data Augmentation for Deep Learning**. *J Big Data*. 2019; **6**: 60.  
[Publisher Full Text](#)
- Stylianiidou S, Brennan C, Nissen SB, et al.: **SuperSegger: Robust Image**

**Segmentation, Analysis and Lineage Tracking of Bacterial Cells.** *Mol Microbiol.* 2016; **102**(4): 690–700.

[PubMed Abstract](#) | [Publisher Full Text](#)

Van Valen DA, Kudo T, Lane KM, *et al.*: **Deep Learning Automates the Quantitative Analysis of Individual Cells in Live-Cell Imaging Experiments.** *PLoS Comput Biol.* 2016; **12**(11): e1005177.

[PubMed Abstract](#) | [Publisher Full Text](#) | [Free Full Text](#)

Weigert M, Schmidt U, Haase R, *et al.*: **Star-Convex Polyhedra for 3D Object Detection and Segmentation in Microscopy.** In: *2020 IEEE Winter Conference*

*on Applications of Computer Vision (WACV).* 2020; 3655–62.

[Publisher Full Text](#)

Zhang M, Zhang J, Wang Y, *et al.*: **Non-Invasive Single-Cell Morphometry in Living Bacterial Biofilms.** *Nat Commun.* 2020; **11**(1): 6151.

[PubMed Abstract](#) | [Publisher Full Text](#) | [Free Full Text](#)

Zhang Y, Ducret A, Shaevitz J, *et al.*: **From Individual Cell Motility to Collective Behaviors: Insights from a Prokaryote, *Myxococcus Xanthus*.** *FEMS Microbiol Rev.* 2012; **36**(1): 149–64.

[PubMed Abstract](#) | [Publisher Full Text](#)